Electronic supplementary information

Partial S substitution activates $NiMoO_4$ for efficient and stable electrocatalytic urea oxidation

Wen-Kai Han, Xiao-Peng Li, Li-Na Lu, Ting Ouyang, Kang Xiao,* and Zhao-Qing Liu*

School of Chemistry and Chemical Engineering/Institute of Clean Energy and Materials/Guangzhou Key Laboratory for Clean Energy and Materials/Key Laboratory for Water Quality and Conservation of the Pearl River Delta, Ministry of Education, Guangzhou University, Guangzhou 510006, China

† *E-mail: kxiao@gzhu.edu.cn; lzqgzu@gzhu.edu.cn (Z. Q. Liu)*

Methods

Synthesis of Preparation of Nickel Molybdate Precursor Grown on Nickel Foam ($NiMoO_4$/NF). Nickel foam was cleaned by dilute hydrochloric acid and then washed in succession with deionized water, ethanol, and acetone several times. For the preparation of metal solution, 0.25 mmol of $(NH_4)_6Mo_7O_{24}$, 0.27 mmol of NH_4F were first dissolved in 30 mL of a mixed solution consisted of 10 mL of deionized water and 20 mL of absolute ethanol and stirred vigorously for 1 h. After that, a cleaned Nickel Foam substrate (1 cm × 3 cm) was immersed into the above solution and the solution was transferred into a 45 mL Teflon-lined stainless-steel autoclave and maintained at 150 °C for 10 h. After the autoclave cooled slowly to room temperature, the sample was taken out and washed with water and ethanol thoroughly, followed by vacuum drying at 60 °C for 12 h and slowly cooled to ambient temperature. The obtained yellowish green sample was named as $NiMoO_4$/NF.

Preparation of S-Substituting Nickel Molybdate ($NiMoO_3S$/NF). The $NiMoO_3S$/NF samples were prepared by heating the above $NiMoO_4$/NF and 6.5 mmol Thiourea at 250 °C under an N_2 atmosphere for 2 h and then cooled to room temperature naturally. To obtain the atomically substituting sample, a slow ramping up and down rate of 1 °C min^{-1} was applied. After annealing process, product was taken out and washed with water and ethanol thoroughly, followed by vacuum drying. The obtained products were name as $NiMoO_3S$/NF and collected for further characterization and electrochemical measurements. The compare samples were obtained at different annealing time or temperature.

Material Characterizations. The field-emission scanning electron microscopy (FE-SEM) images were performed on a JEOL JSM-7001F SEM instrument. Transmission electron microscopy (TEM) and high-resolution TEM (HRTEM) were carried out on a Tecnai G2 F20 S-TWIN field-emission electron microscope operated at an acceleration voltage of 200 kV. The phase composition of samples was analyzed by X-ray diffraction (XRD, Bruker, D8 ADVANCE) with Cu Kα radiation (λ = 1.5418 Å). XPS was conducted on a Thermo Scientific™ K-Alpha™+ spectrometer equipped with a monochromatic Al Kα X-ray source (1486.6 eV) operating at 100 W. Samples were analysed under vacuum ($P < 10^{-8}$ mbar) with a pass energy of 150 eV (survey scans) or 25eV (high-resolution scans). All peaks were calibrated with C1s peak binding energy at 284.8 eV for adventitious carbon. The experimental peaks were fitted with Advantage software.

Electrochemical Tests. The electrochemical performance of the UOR was tested in a three-electrode system on an electrochemical workstation (CHI760E). An Hg/HgO (saturated KOH solution) electrode was used as the reference electrode, while the counter electrode was graphite rod electrode. For the 3D electrode, the as-obtained

$NiMoO_3S$/NF was directly used as the working electrode for the electrochemical tests in the solution (1 M KOH + 0.5 M urea). The CV plots were recorded at scan rates of 5–100 mV s^{-1}. The working electrodes were first activated by CV cycling for several times until stabilization was reached before data collection. EIS measurements of the catalysts were performed at a potential of 0 V *vs.* RHE by using an ac voltage with 5 mV amplitude in a frequency range from 1000 kHz to 1 Hz. The electrode stability was tested by both CV and chronoamperometric response. All measured potentials were reported versus reversible hydrogen electrode (RHE) according to the equation:

$$E_{RHE} = E_{Hg/HgO} + 0.098 + 0.059 \times pH \quad (1)$$

The corrected oxidation and reduction peaks to calculate the oxidation and reduction weighted centers according to the equation:

$$V_{weighted} = \int V dQ / \int dQ \quad (2)$$

where Q is the corresponding charge transfer at the voltage V in the redox process. The average value of the oxidation and reduction weighted centers was used as the redox weighted center.[30]

Based on the CV measurements at different scanning rates (2, 4, 6, 8, 10 mV s^{-1}) to get the C_{dl} of the catalyst, the ECSA was obtained according to the following equation:

$$ECSA = C_{dl}/C_s \quad (3)$$

where C_s represents the specific capacitance. EIS was measured at a bias potential of 0 V (*vs.* Hg/HgO) and in a frequency range from 0.1 to 106 Hz.

Calculation Details. The Density Functional Theory (DFT) calculations in this work are carried out using the Vienna ab-initio simulation package (VASP, version 5.4.4) code.[1] The PBE functional was employed for electronic exchange and correlation. The plane wave pseudopotential with a kinetic cutoff energy of 500 eV and Gaussian smearing method with an electronic temperature of k_BT = 0.05 eV were used in the calculations. In the geometrical optimization process was stopped when the total electronic energies were converged to 10^{-6} eV and the residual forces on the atoms were converged to 0.02 eV $Å^{-1}$.[2]

In our models, the unit cell of $NiMoO_4$ contained 8 Ni atoms, 8 Mo atoms and 32 O atoms. The unit cell of $NiMoO_3S$ was constructed by substituting 8 equivalent O atoms for 8 S atoms. During relaxing process, Brillouin-zone integration was conducted using a 7 × 7 × 7 Monkhorst-Pack grid.[3] The surfaces were simulated by slab models and cleaved along (110) facet based on the XRD data. A ~ 10 Å thick vacuum space was added to avoid inter-layer interactions. Brillouin-zone integration was conducted using a 7 × 7× 1 Monkhorst-Pack grid. In the geometrical optimization, the top three atom layers and the associated adsorbates were allowed to relax while the other atoms were fixed.

The binding energy (E_{BE}) of the adsorbates is defined as: $E_{BE} = E_{tot} - E_{sub} - E_{ads}$, where E_{tot}, E_{sub} and E_{ads} are the total energy of optimized adsorbate + substrate, clean substrate and gas phase adsorbate respectively, and they can be directly obtained from DFT calculations. Charge density difference (CDD) of urea adsorbed $NiMoO_4$ and $NiMoO_3S$ is calculated as $\Delta\rho = \rho_{tot} - \rho_{sub} - \rho_{ads}$, where ρ_{tot}, ρsub and ρads are charge density of the bonded adsorbate and substrate, independent clean substrate and adsorbate respectively.

Supplementary Figures

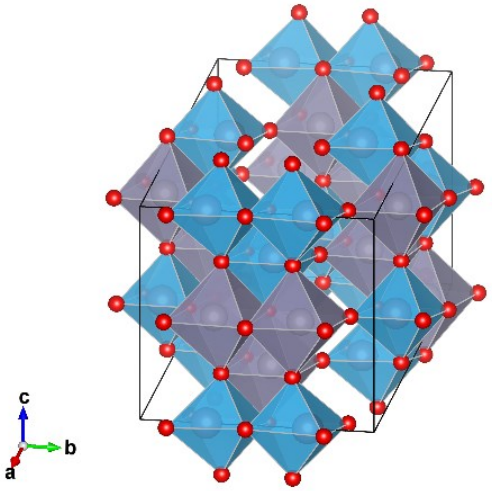

Figure S1. The crystal structure of $NiMoO_4$.

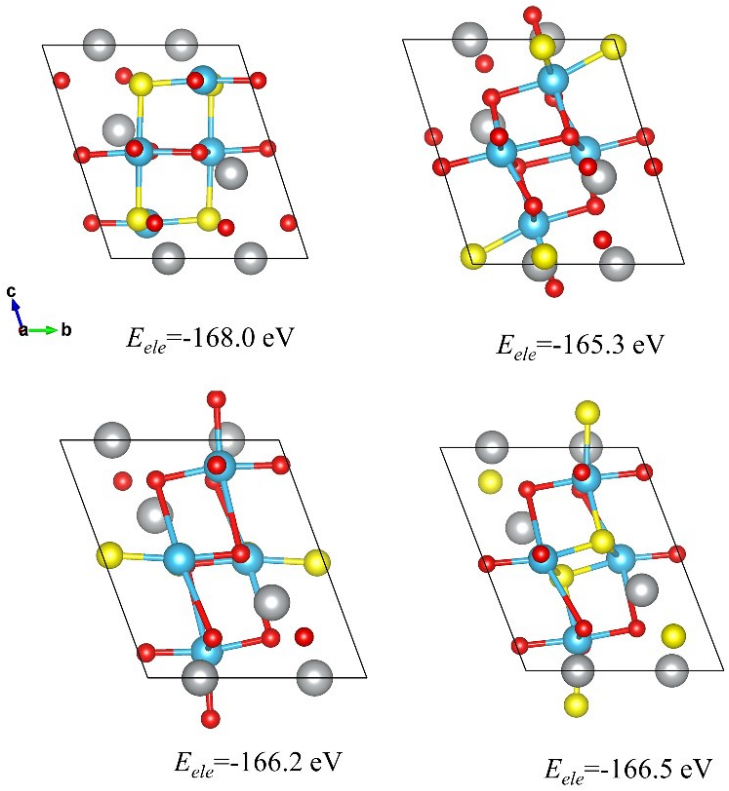

Figure S2. Schematic diagram of substituted S on the four different symmetric positions in $NiMoO_4$.

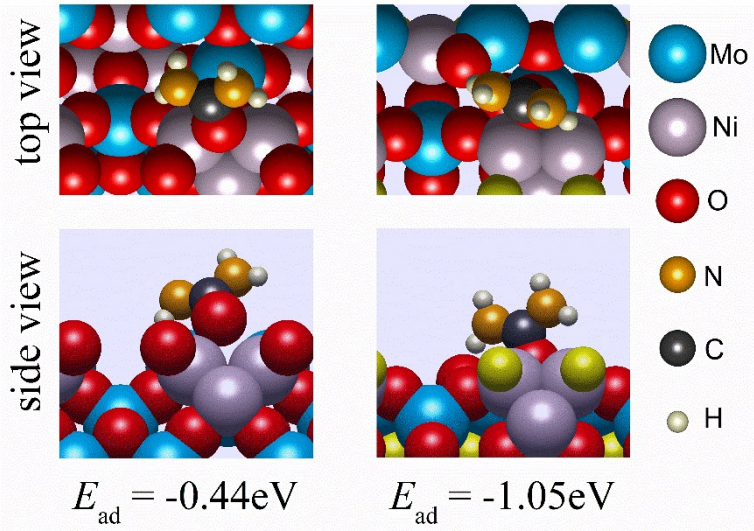

Figure S3. Model of adsorption of urea molecules on Ni sites with the case of the O of a urea molecule is bonded to Ni site on the surface.

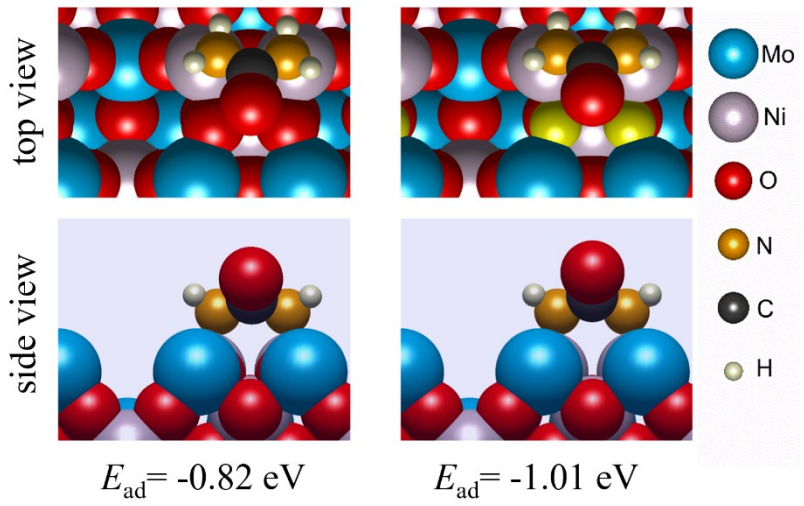

Figure S4. Model of adsorption of urea molecules on Ni sites with the case of the N of a urea molecule is bonded to Ni site on the surface.

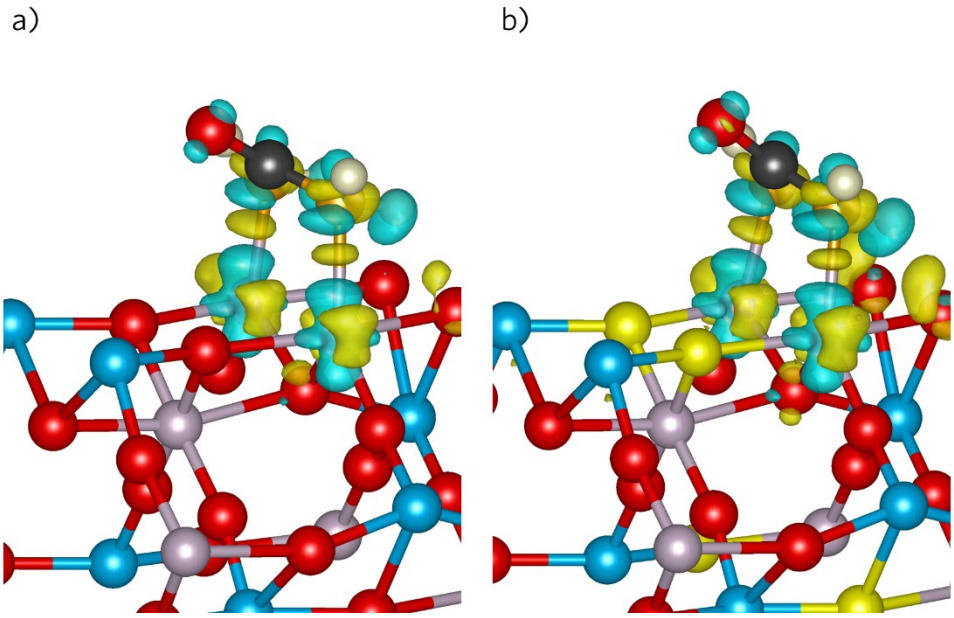

Figure S5. The Schematic diagram of CDD of a) $NiMoO_4$ and b) $NiMoO_3S$, which is obtained with the case of the N of a urea molecule is bonded to Ni site on the surface.

The urea adsorption energy of $NiMoO_4$ in this adsorption mode was calculated to be higher than that of $NiMoO_4$ in the Ni–O mode, while the urea adsorption energy of $NiMoO_3S$ in the Ni–N binding mode was lower than that of $NiMoO_3S$ in the in the Ni–O mode, and the difference between the charge differential density of the unsubstituted molecule and that of the partially substituted one was not obvious.

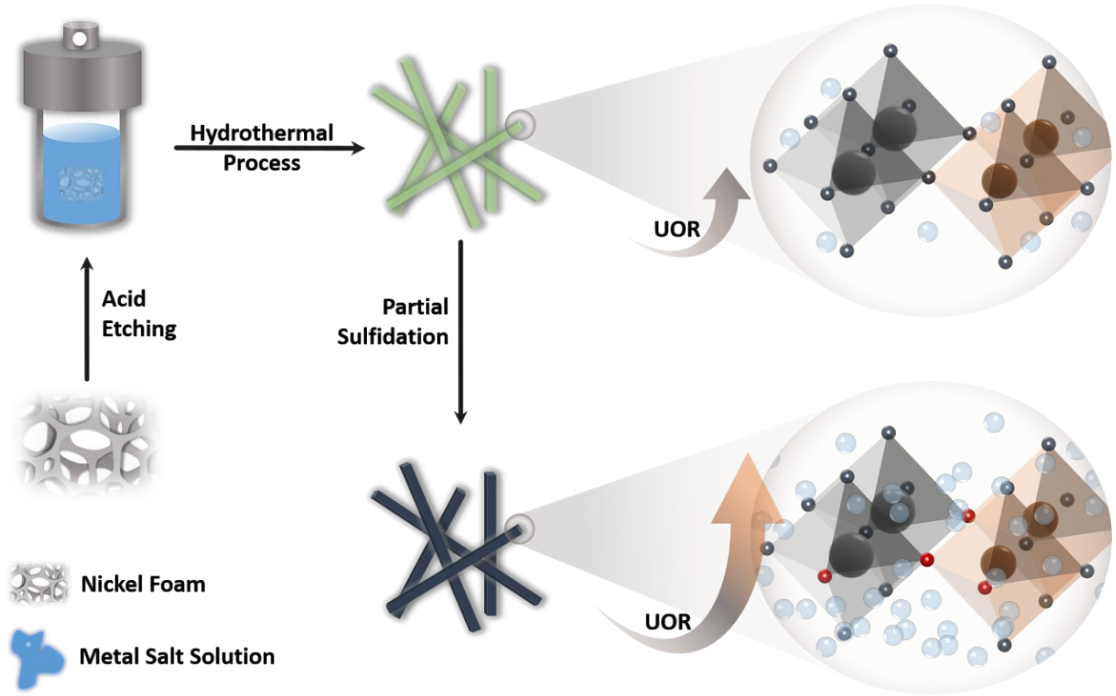

Scheme S1. Schematic illustration for the synthesis of NiMoO4/NF and $NiMoO_3S$/NF.

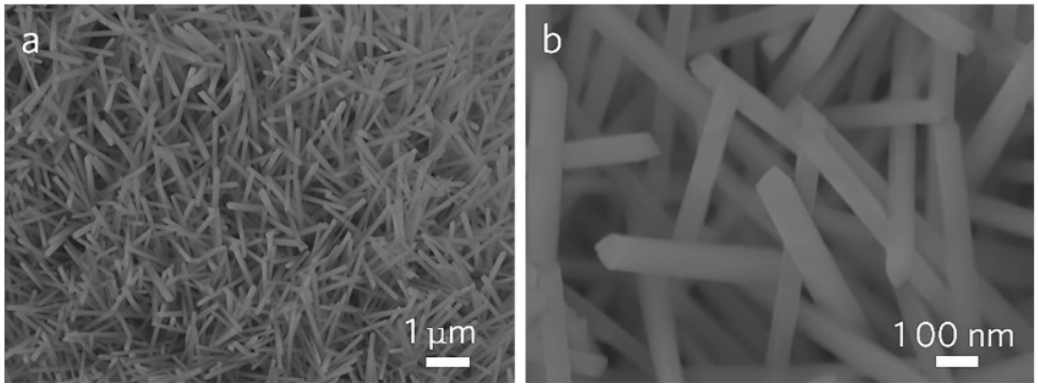

Figure S6. SEM images of $NiMoO_4$/NF nanorods at low magnification and high magnification.

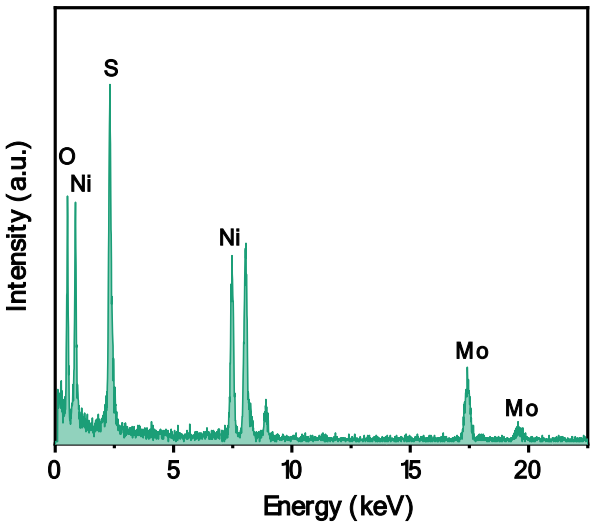

Element	Weight %	Atomic %
O	15.81	41.40
S	12.98	16.96
Ni	19.41	13.86
Mo	23.10	15.23

Figure S7. The element atomic content of Ni, Mo and O elements in the $NiMoO_3S$/NF.

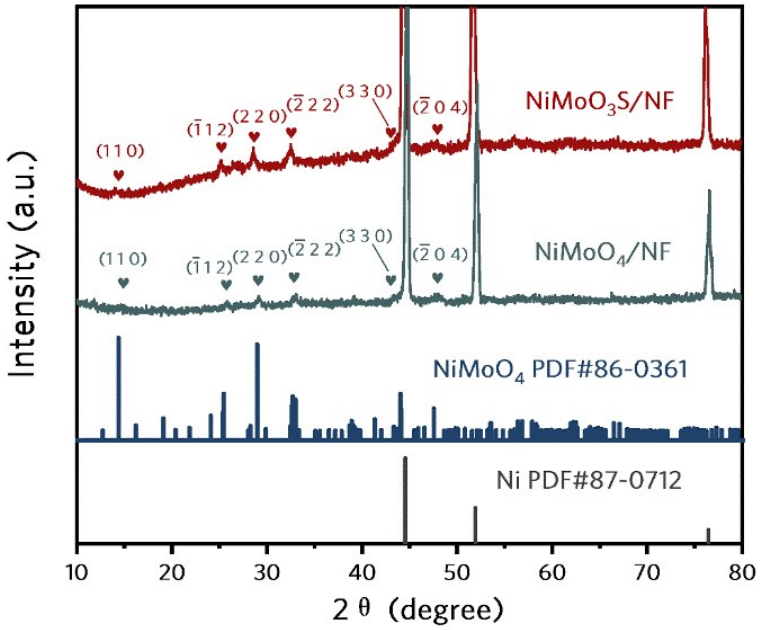

Figure S8. XRD of $NiMoO_4$/NF, $NiMoO_3S$/NF.

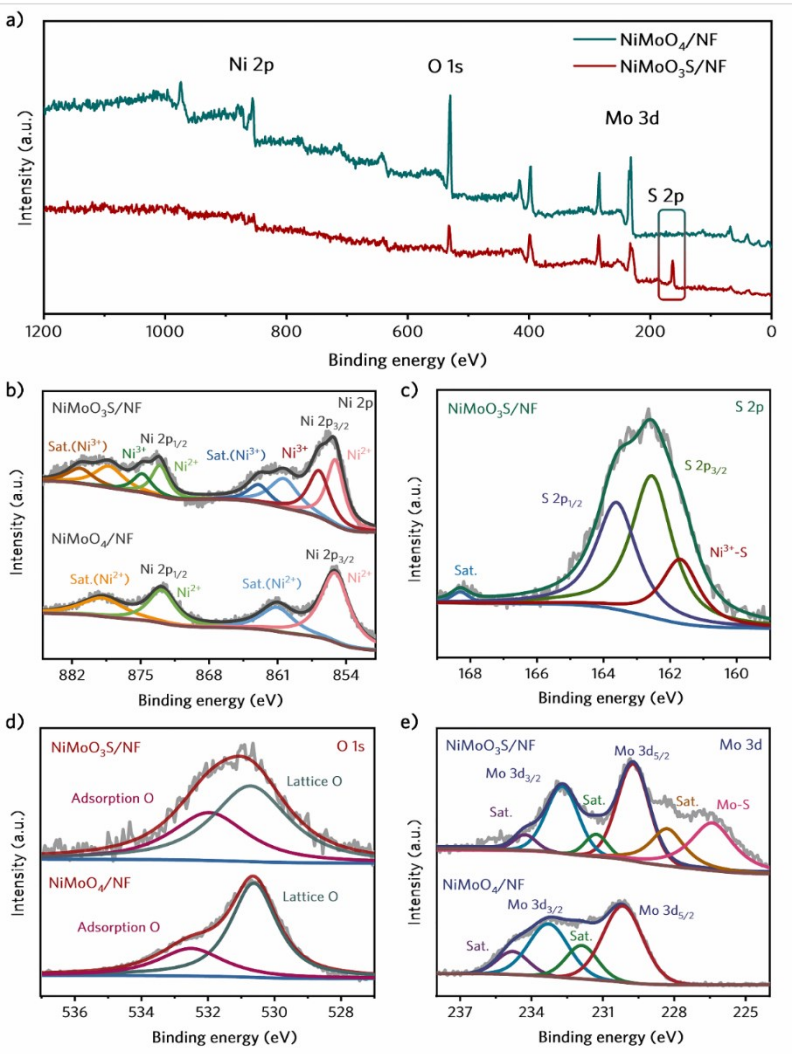

Figure S9. (a) Survey XPS spectra of $NiMoO_4$/NF and $NiMoO_3S$/NF. XPS spectra of b) Ni 2p, c) S 2p, d) O 1s and e) Mo 3d.

The survey XPS spectra confirmed the presence of Ni, Mo and O elements in $NiMoO_4$/NF and Ni, Mo, O and emerging S in $NiMoO_3S$/NF (Figure S9a). As shown in Figure S9b and S9c, the emerged peaks, at 856.85 eV assigned to signals of Ni^{3+} and at 161.70 eV assigned to signals of Ni^{3+}-S bond, confirms that this optimization of the coordination around nickel caused by S substitution.[4] [5]. In the high-resolution spectrum of O 1s, the electron binding energies of the lattice O have a negative shift of about 0.6 eV after S substitution, indicating the charge transfer from S to O (Figure S9d).[6] In Figure S9e, the Mo 3d spectra were divided into three peaks corresponding to Mo $3d_{3/2}$, Mo $3d_{1/2}$ and Mo-S bond (at 226.45 eV), respectively.[7]

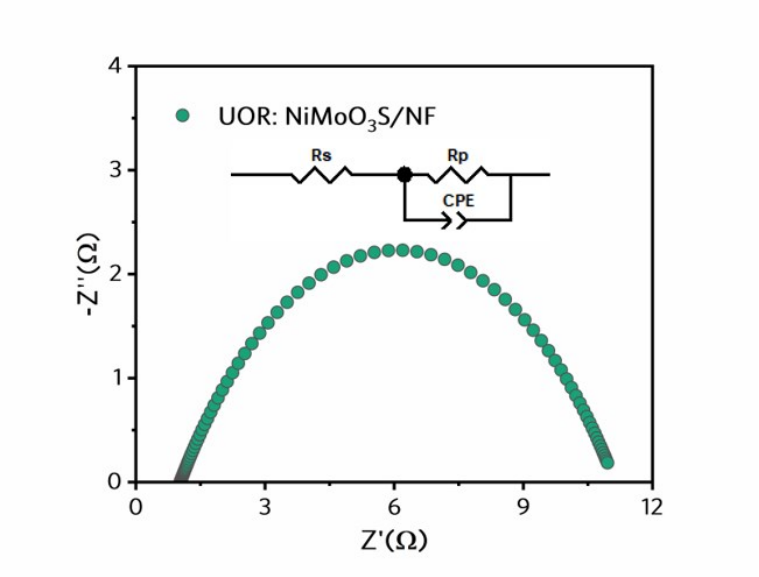

Figure S10. The corresponding fitting Nyquist plots for $NiMoO_3S$/NF. Inset in (b) is the equivalent circuit. The equivalent circuit was consisted of a resistor (R_s) in series with one parallel combinations of a resistor (R_p) and a constant phase element (CPE), in which R_s represents the uncompensated solution resistance, the time constant R_p-CPE may relate to the interfacial resistance.

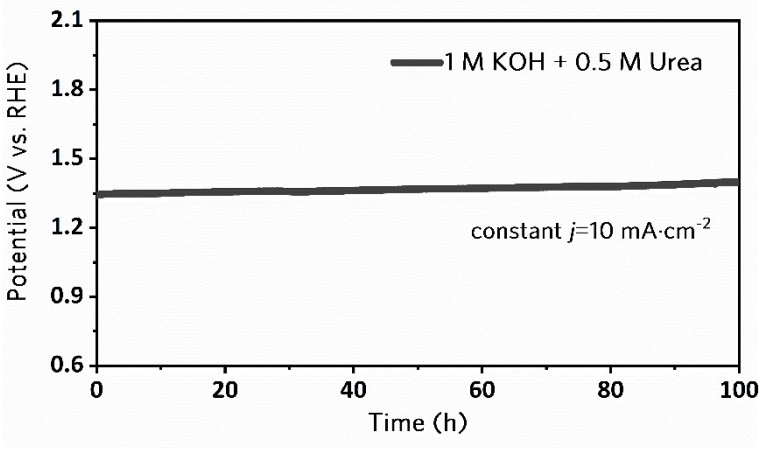

Figure S11. Galvanostatic measurement of $NiMoO_3S$/NF catalyst at a constant current density for 100 h.

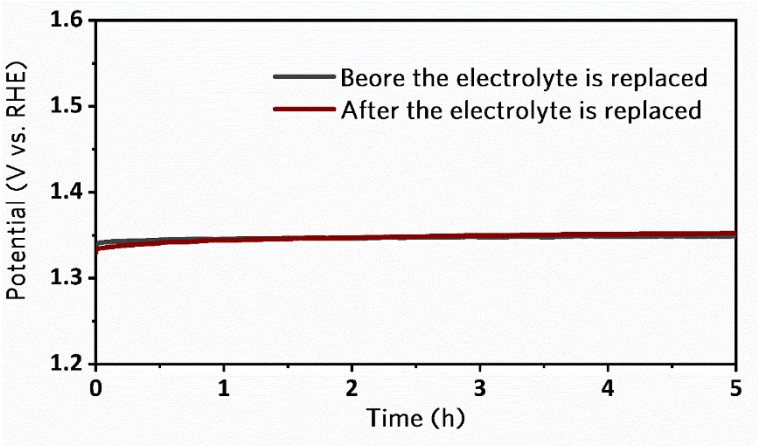

Figure S12. Galvanostatic measurement of $NiMoO_3S$/NF catalyst after the electrolyte is replaced. The data of gray line was obtained during the first 5 h of the 100-h test period, and the data of red line was obtained by replacing the electrolyte after the test for 100 h.

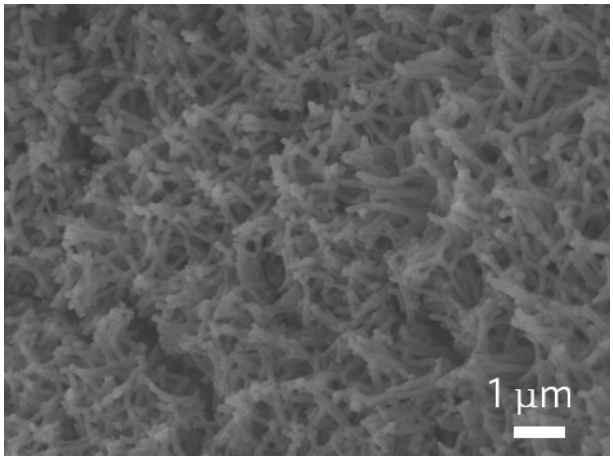

Figure S13. SEM of $NiMoO_3S$/NF after galvanostatic measurement for 100 h.

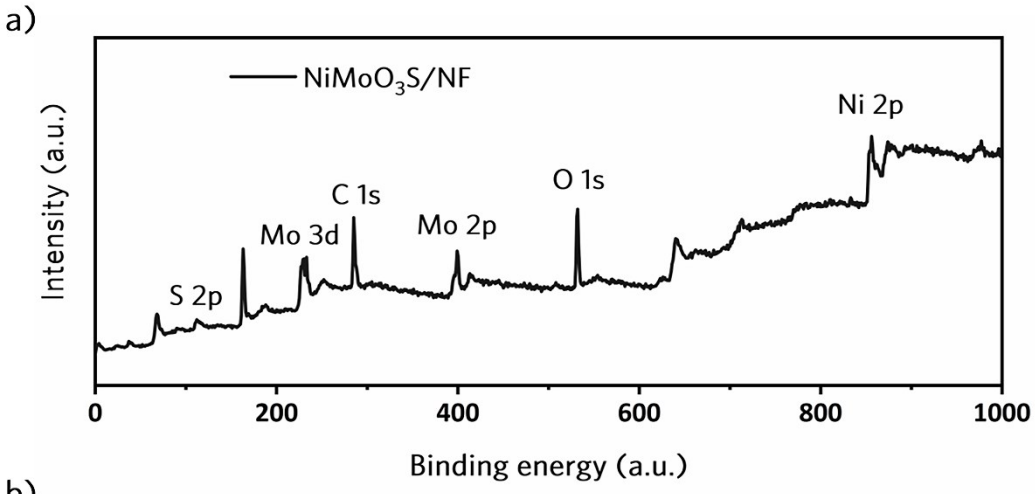

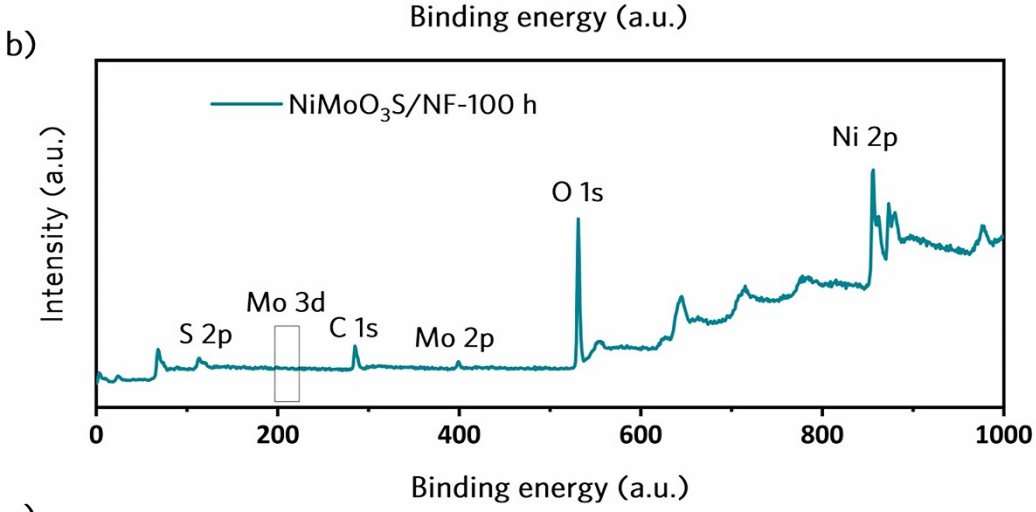

c)

Sample	Elements atomic ratio (%)			
	Ni	Mo	O	S
$NiMoO_3S$/NF	9.56	5.95	19.95	21.93
$NiMoO_3S$/NF-100 h	23.43	0.24	50.35	1.05

Figure S14. The XPS survey of (a) $NiMoO_3S$/NF and (b) $NiMoO_3S$/NF-100 h samples. (c) The element atomic content of Ni, Mo, O and S elements in the $NiMoO_3S$/NF and $NiMoO_3S$/NF-100 h products.

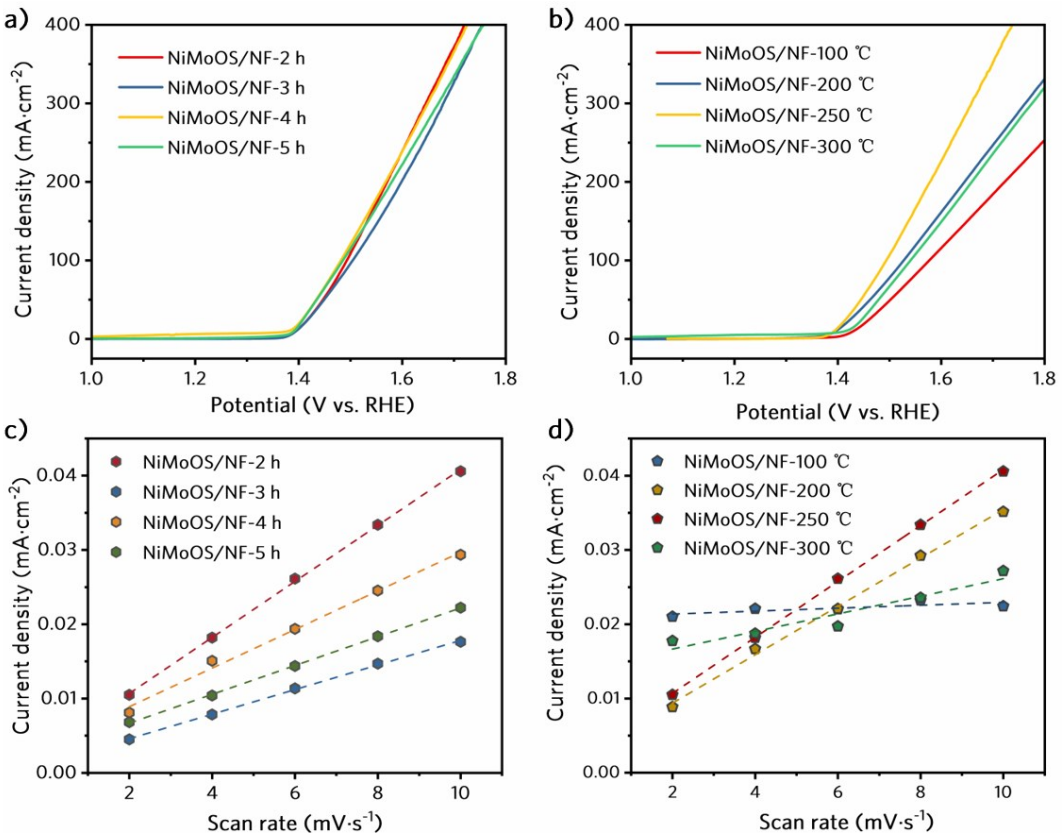

Figure S15. (a) C_{dl} and (c) LSV of series of series of .NiMoOS/NF for 2 h, 3 h, 4 h, 5 h; (b) C_{dl} and (d) LSV of Ni-Mo-O-S at 200 °C, 250 °C, 300 °C, which were recorded in 0.5 M Urea with 1 M KOH at normal condition.

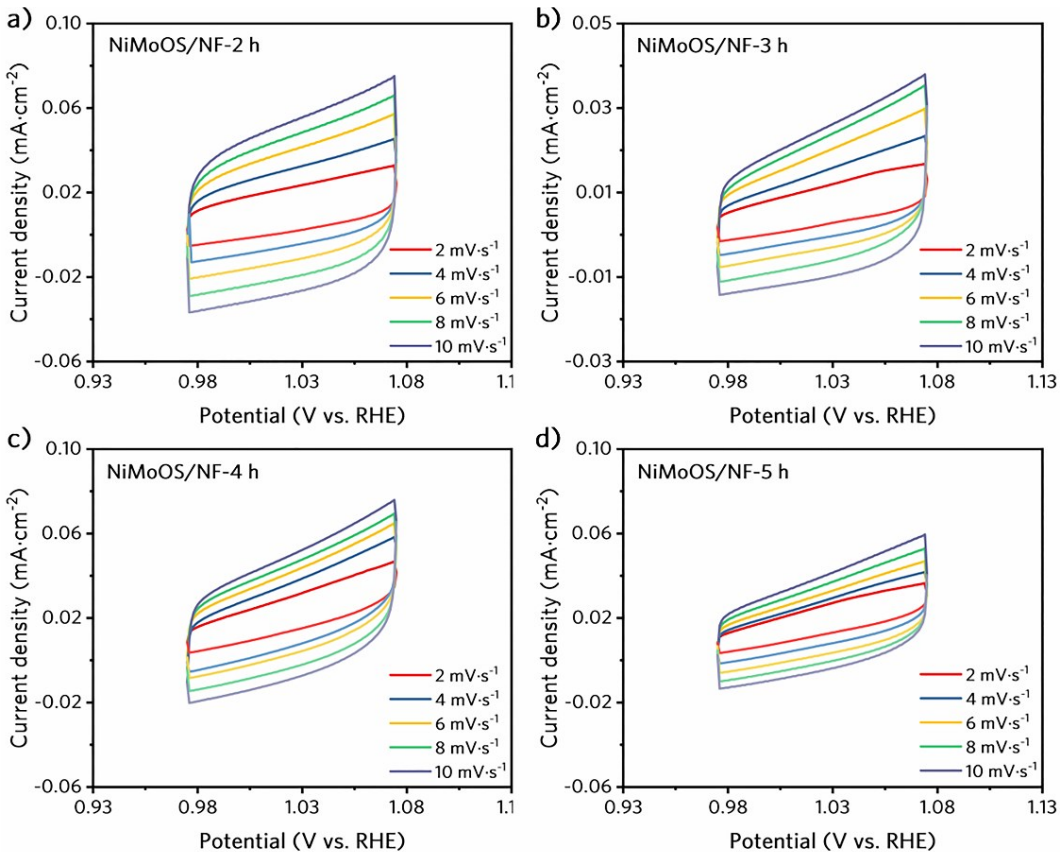

Figure S16. (a–d) CV curves of series of NiMoOS/NF for 2 h, 3 h, 4 h, 5 h at scan rates from 2 to 10 $mV \cdot s^{-1}$, which were recorded in 0.5 M Urea with 1 M KOH at normal condition.

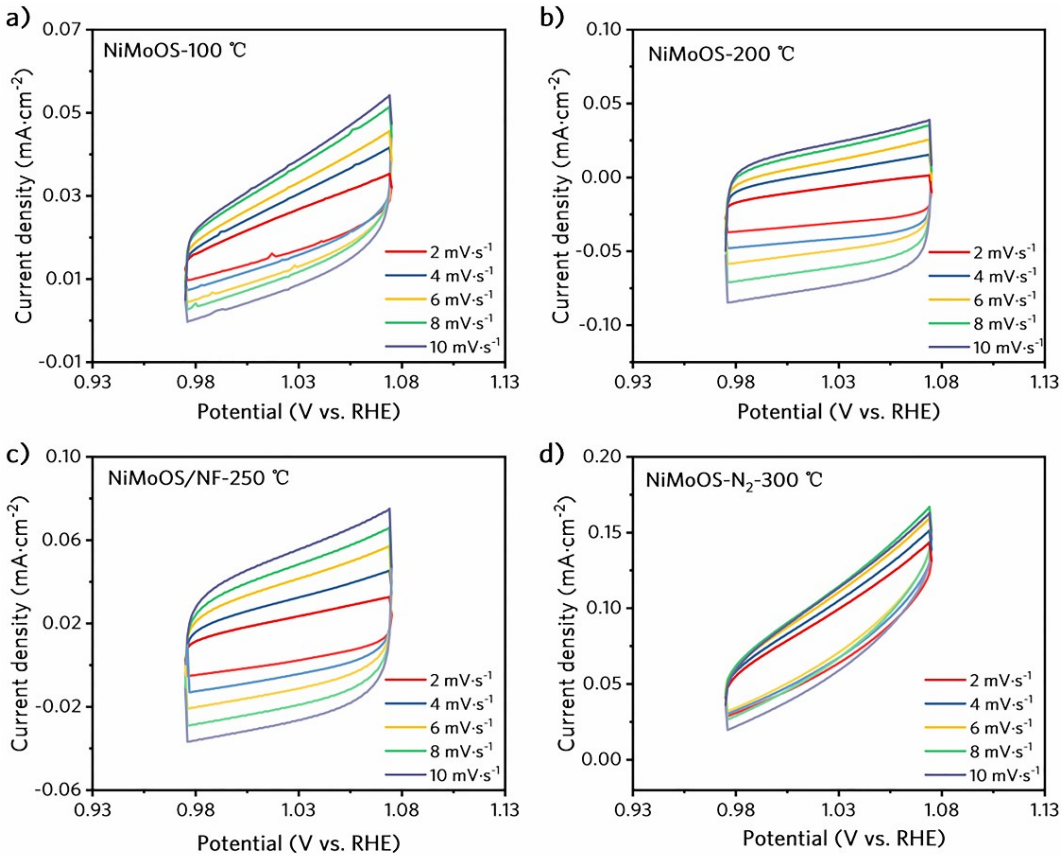

Figure S17. (a–d) CV curves of series of NiMoOS/NF at 100°C, 200 °C, 250 °C, 300 °C at scan rates from 2 to 10 $mV \cdot s^{-1}$, which were recorded in 0.5 M Urea with 1 M KOH at normal condition.

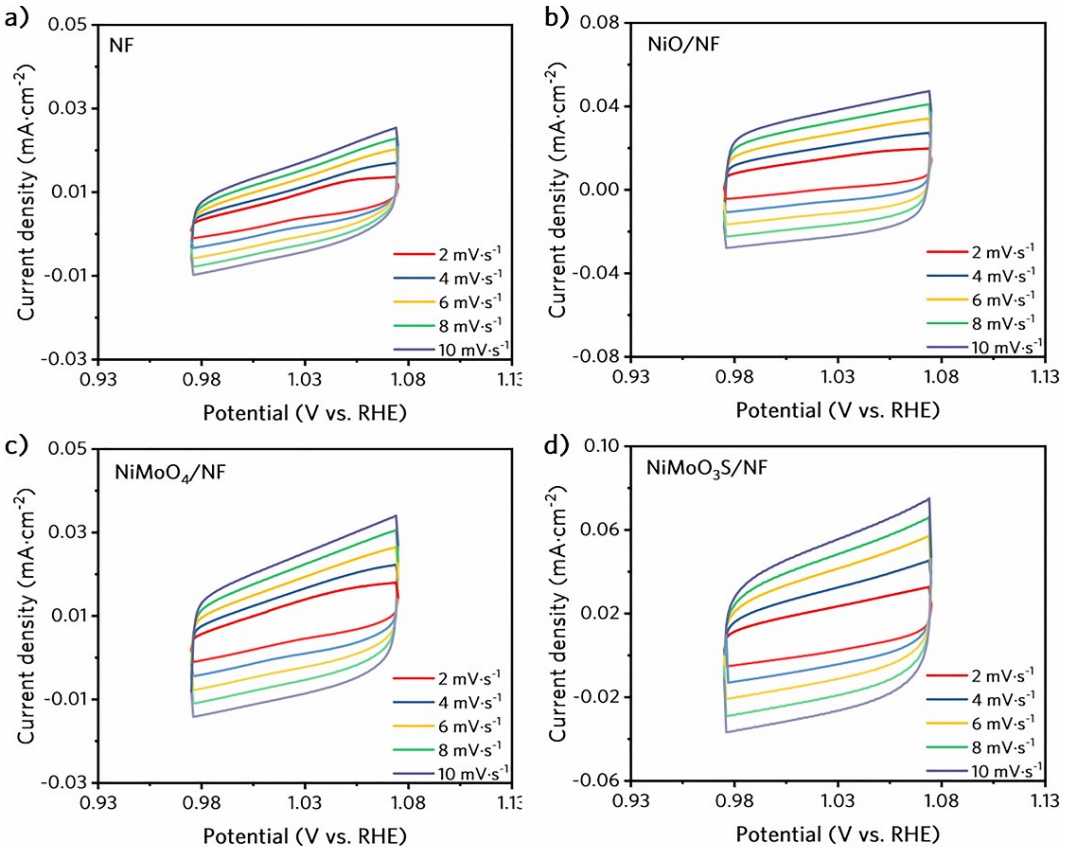

Figure S18. (a–d) CV curves of NF, NiO/NF, $NiMoO_4$/NF, $NiMoO_3S$/NF at scan rates from 2 to 10 $mV \cdot s^{-1}$, which were recorded in 0.5 M Urea with 1 M KOH at normal condition.

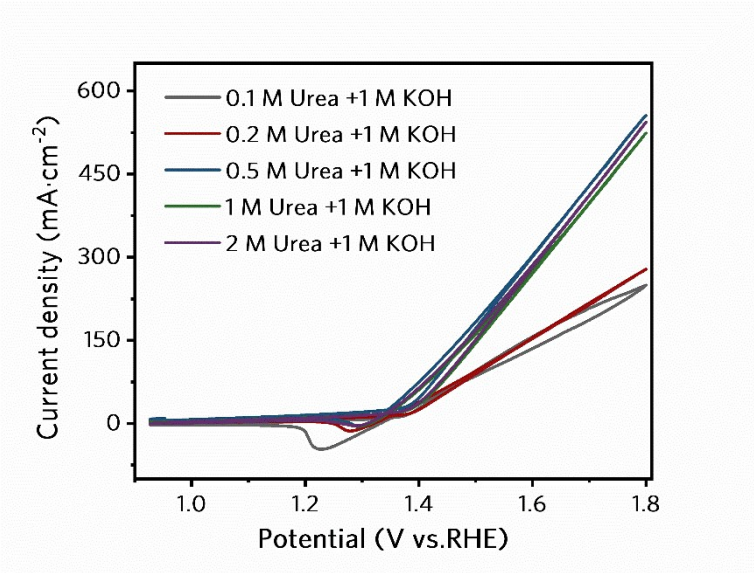

Figure S19. CVs of $NiMoO_3S$/NF in 1 M KOH with different concentration from 0.1 to 2 M of Urea.

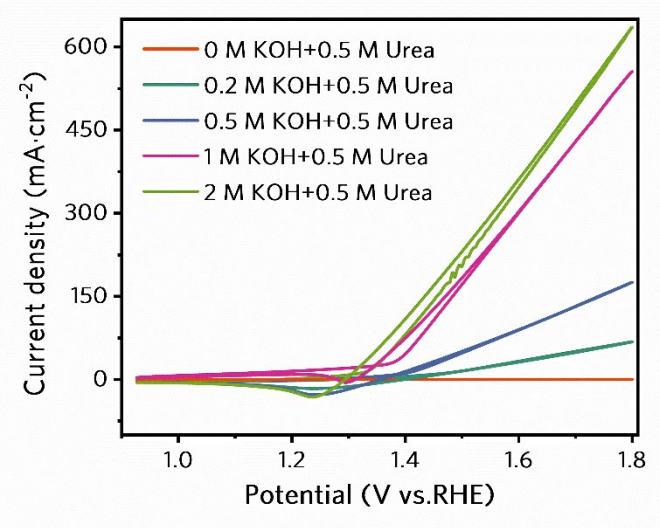

Figure S20. CVs of $NiMoO_3S$/NF in 0.5 M Urea with different concentration from 0 to 2 M of KOH.

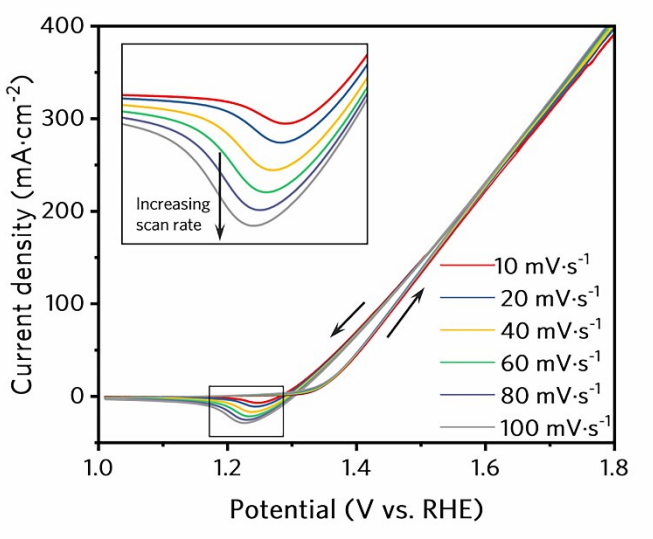

Figure S21. Cyclic voltammetry plots for $NiMoO_3S$/NF at scan rates from 10 to 100 $mV \cdot s^{-1}$, which were recorded in 0.5 M Urea with 1 M KOH at normal condition.

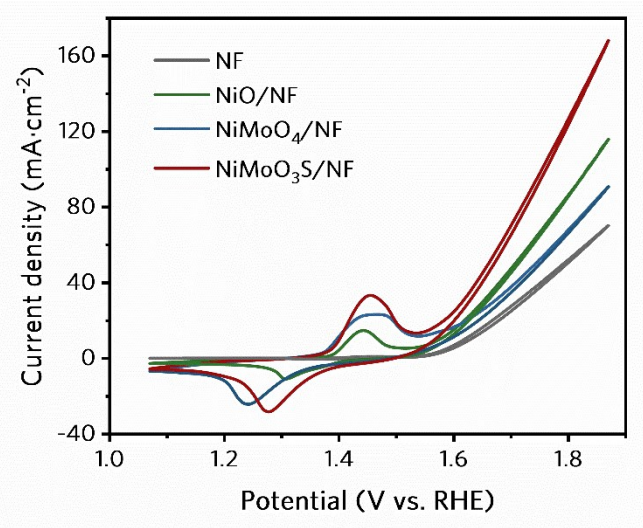

Figure S22. CVs of Nickle Foam, NiO/NF, $NiMoO_4$/NF, $NiMoO_3S$/NF in 1 M KOH.

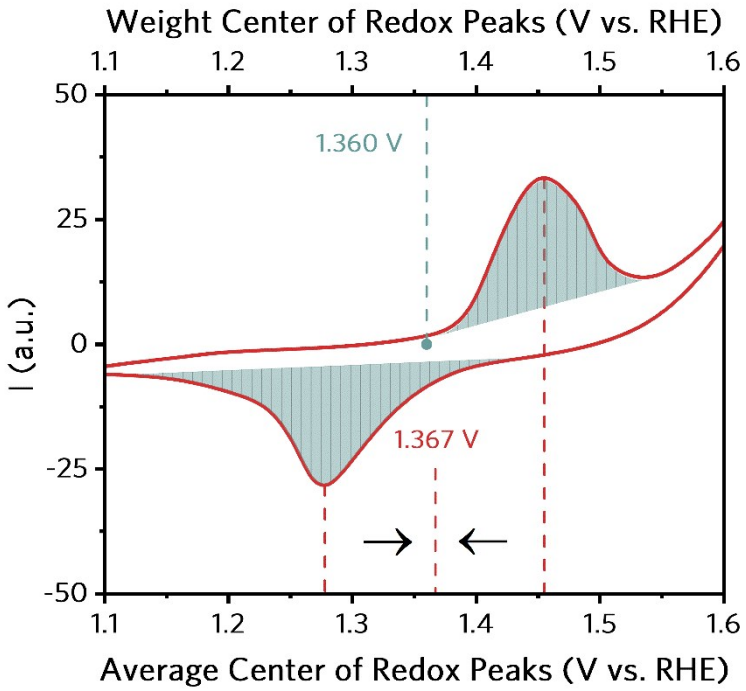

Figure S23. The calculations of the weighted center and average center position of redox peaks for $NiMoO_3S$/NF. Firstly, the linear double-layer-capacitance background corrections were applied to extract the oxidation and reduction peaks, respectively. Second, function $V_{weighted} = \int V dQ / \int dQ$ was applied on the corrected oxidation and reduction peaks to calculate the oxidation and reduction weighted centers, where Q is the corresponding charge transfer at the voltage V in the redox process. At last, the average value of the oxidation and reduction weighted centers was used as the redox weighted center, which is the blue dash line shown in the figure. The red dash lines on the left and right sides show the simple peak positions of the oxidation and reduction processes, while the central red dash line represents the average center position of redox peaks.

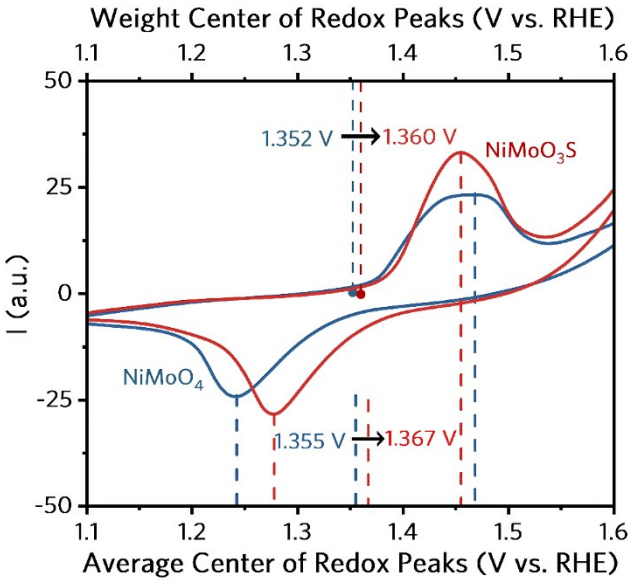

Figure S24. Graphical representation of the calculations of the weighted center and average center position of redox peaks for $NiMoO_4$/NF and $NiMoO_3S$/NF.

References

1 (a) M. Sano, T. Adaniya, T. Fujitani, J. Nakamura, *Surf. Sci.* **2002**, *514*, 261; (b) T. V. Pavlova, B. V. Andryushechkin, G. M. Zhidomirov, *J. Phys. Chem. C* **2016**, *120*, 2829; (c) G. Kresse, J. Furthmüller, *Comp. Mater. Sci.* **1996**, *6*, 15; (d) G. Kresse, J. Furthmüller, *Phys. Rev. B* **1996**, *54*, 11169.

2 J. P. Perdew, K. Burke, Ernzerhof, M. *Phys. Rev. Lett.* **1996**, *77*, 3865.

3 D. J. Chadi, *Phys. Rev. B* **1977**, *16*, 790.

4 (a) M. Li, T. Liu, Y. Yang, W. Qiu, C. Liang, Y. Tong, Y. Li, *ACS Energy Lett.* **2019**, *4*, 1983; (b) Q. He, Y. Wan, H. Jiang, Z. Pan, C. Wu, M. Wang, X. Wu, B. Ye, P. M. Ajayan, L. Song, *ACS Energy Lett.* **2018**, *3*, 1373.

5 T. Tian, H. Gao, X. Zhou, L. Zheng, J. Wu, K. Li, Y. Ding, *ACS Energy Lett.* **2018**, *3*, 2150.

6 An, L.; Zhang, Z.; Feng, J.; Lv, F.; Li, Y.; Wang, R.; Lu, M.; Gupta, R. B.; Xi, P.; Zhang, S. *J. Am. Chem. Soc.* **2018***, 140,* 17624.

7 (a) D. Gopalakrishnan, D. Damien, M. M. Shaijumon, *ACS Nano* **2014**, *8*, 5297; (b) Y. Li, R. Zhang, W. Zhou, X. Wu, H. Zhang, J. Zhang, *ACS Nano* **2019**, *13*, 5533.

Table S1

Sample ID	Electrolyte	Cell Voltage [V]	Current Density [mA cm^{-2}]	Stability	Ref.
$NiMoO_3S$/NF	1.0 M KOH 0.5 M urea	1.340	10	100 h @10 mA·cm^{-2}	This work
NF/NiMoO-Ar **NF/NiMoO-H_2**	1.0 M KOH 0.5 M urea	1.38	10	50 h @ 1.58 V	*Energy Environ. Sci.* 2018, **11**, 1890
Ni–Mo nanotube	1.0 M KOH 0.5 M urea	1.43	10	10 h @10 mA·cm^{-2}	*Nano Energy* 2019, **60**, 894.
r-$NiMoO_4$/NF	1.0 M KOH 0.5 M urea	0.6 V vs. Ag/AgCl	249.5	~5.5 h @ 400 mV	*ACS Catal.* 2018, **8**, 1
Ni-CoP/HPFs	1.0 M KOH 0.5 M urea	1.43	10	25 h	*Nano Energy* 2019, **56**, 411
NiCoP /CC	1.0 M KOH 0.5 M urea	1.42	10	30 h @20 mA·cm^{-2}	*J. Mater. Chem. A* 2019,**7**,9078
Rh-Ni electrode	1.0 M KOH 0.3 M urea	1.40	50	24 h @1.55 V	*J. Power Sources* 2011, **196**, 9579
$Ni_{0.9}Fe_{0.1}O$	1.0 M KOH 0.33 M urea	1.455	10	25 h @ 10 mA·cm^{-2}	*Chem. Commun.* 2019, **55**, 6555
MoS_2/Ni_3S_2	1.0 M KOH 0.33 M urea	1.45	20	20 h @ 20 mA·cm^{-2}	*Chem. Commun.* 2018,**54**, 5181
Ni_3N/NF	1.0 M KOH 0.5 M urea	1.42	100	20 h	*ACS Appl. Mater. Interfaces* 2019, **11**, 13168
Mo-Co-S-Se/CC	1.0 M KOH 0.5 M urea	1.40	10	11 h @ 10 mA·cm	*ACS Sustainable Chem. Eng.* 2019, **7**, 16577
NiTe/rGO/NF	1.0 M KOH 0.33 M urea	1.50	10	9.7 h @40 mA·cm^{-2}	*ACS Appl. Energy Mater.* 2019, **2**,3363